1	
2	
3	Adsorption Behavior of Long-Chain Perfluoroalkyl
4	Substances on Hydrophobic Surface: A Combined
5	Molecular Characterization and Simulation Study
6	
7	by
8	Tashfia M. Mohona, <sup>1,3</sup> Zhijiang Ye, <sup>2</sup> Ning Dai, <sup>1*</sup> and Prathima C. Nalam <sup>3*</sup>
9	
10 11	<sup>1</sup> Department of Civil, Structural and Environmental Engineering, University at Buffalo, Buffalo, NY, USA
12 13	<sup>2</sup> Department of Mechanical and Manufacturing Engineering, Miami University, Oxford, OH, USA
14 15	<sup>3</sup> Department of Materials Design and Innovation, University at Buffalo, Buffalo, NY, USA
16	
17	
18	Submitted
19 20	to Water Research (May 2023)
21	water research (way 2020)
22	
23	
24	<sup>1,*</sup> Corresponding Author: Ning Dai, Phone: (716) 645-4015, Email: ningdai@buffalo.edu
25	<sup>3,*</sup> Corresponding Author: Prathima C. Nalam, Phone: (716) 645-9193, Email: prathima@buffalo.edu
26	
27	

- 28 Keywords: PFAS sorption, hydrophobic surfaces, self-assembled monolayer (SAM), quartz
- 29 crystal microbalance (QCM), atomic force microscopy (AFM), molecular dynamics (MD)
- 30 simulation

# 31 Highlights:

- PFNA/PFOS adsorption on hydrophobic CH<sub>3</sub>- SAM was studied using QCM, AFM, and MD
- Adsorbed PFNA/PFOS molecules lay flat/aggregated on or tail-inserted into SAM
- PFNA is adsorbed more than PFOS but forms fewer aggregates/structures on surface

37

38

39

40

41

42

43

44

45

46

47

48

49

50

51

52

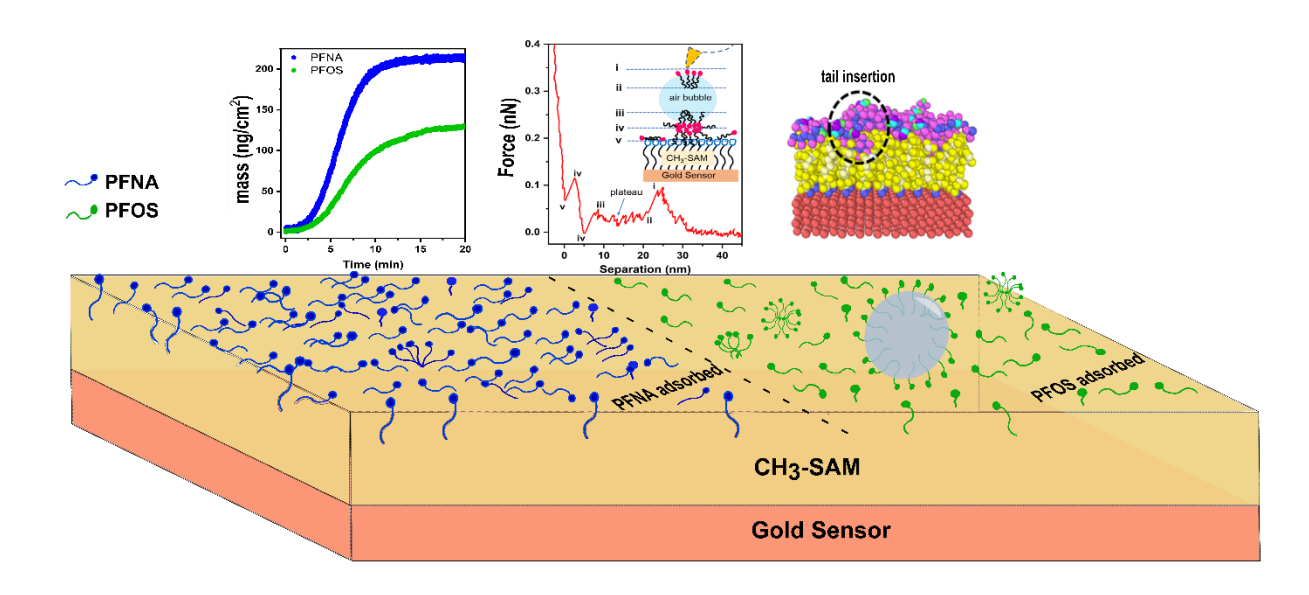
53

54

#### Abstract

Hydrophobic interaction is a prevalent sorption mechanism of poly- and perfluoroalkyl substances (PFAS) in natural and engineered environments. In this study, we combined quartz crystal microbalance with dissipation (QCM-D), atomic force microscope (AFM) with force mapping, and molecular dynamics (MD) simulation to probe the molecular behavior of PFAS at the hydrophobic interface. On a CH<sub>3</sub>-terminated self-assembled monolayer (SAM), perfluorononanoic acid (PFNA) showed ~2-fold higher adsorption than perfluorooctane sulfonate (PFOS) that has the same fluorocarbon tail length but a different head group. Kinetic modeling using the linearized Avrami model suggests that the PFNA/PFOS-surface interaction mechanisms can evolve over time. This is confirmed by AFM force-distance measurements, which shows that while the adsorbed PFNA/PFOS molecules mostly lay flat, a portion of them formed aggregates/hierarchical structures of 1–10 nm in size after lateral diffusion on surface. PFOS showed a higher affinity to aggregate than PFNA. Association with air nanobubbles is observed for PFOS but not PFNA. MD simulations further showed that PFNA has a greater tendency than PFOS to have its tail inserted into the hydrophobic SAM, which can enhance adsorption but limit lateral diffusion, consistent with the relative behavior of PFNA/PFOS in QCM and AFM experiments. This integrative QCM-AFM-MD study reveals that the interfacial behavior of PFAS molecules can be heterogeneous even on a relatively homogeneous surface.

# **Graphical Abstract**



#### 1. Introduction

Poly- and perfluoroalkyl substances (PFAS) are a group of synthetic organic compounds widely used as surfactants in consumer products and firefighting (Buck et al., 2011; Moody and Field, 2000). These compounds can persist in the environment (Evich et al., 2022) and bioaccumulate in the food chain (Conder et al., 2008). They have been found in surface water and groundwater at levels above human and ecological health thresholds (CDC, 2019; Sunderland et al., 2019). The strong C-F bonds in PFASs (bond dissociation energy of 485 kJ mol<sup>-1</sup> (O'Hagan, 2008)) contribute to their resistance to degradation in both natural and engineered systems (Mahinroosta and Senevirathna, 2020; McCleaf et al., 2017).

Sorption plays an important role in determining the natural fate of PFAS (Lyu et al., 2022) as well as for developing sorption-based PFAS removal processes for water treatment, such as activated carbon sorption (McCleaf et al., 2017) and ion exchange (Boyer et al., 2021). However, the amphiphilic and oleophobic characteristics of PFASs render it difficult to accurately predict their sorption based on surface and solution conditions (Deng et al., 2012; Zhang et al., 2019). For example, when attempting to correlate PFAS sorption with the bulk properties of soil/sediment, such as organic fraction, protein content, anion or cation exchange capacity, and mineral type, the co-variation of these properties in the sorbent has been shown to lead to confounding results (Ebrahimi et al., 2021; Gagliano et al., 2020; Li et al., 2019; Li et al., 2018). Soil/sediment organic content, a classic parameter to predict the sorption of legacy organic contaminants, was found to positively correlate with PFAS sorption in some studies (Guelfo and Higgins, 2013; Higgins and Luthy, 2006; Jeon et al., 2011; Li et al., 2019; Milinovic et al., 2015; Qian et al., 2017; Wei et al., 2017; You et al., 2010) but not in others (Barzen-Hanson et al., 2017; Lee and Mabury, 2017; Li et al., 2018; Pan and You, 2010). For most engineered sorbents, hydrophobic and electrostatic

interactions drive PFAS sorption (Gagliano et al., 2020), but other interaction mechanisms such as van der Waals forces, hydrogen bonding, and ligand exchange can also contribute, especially if hydrophobic/electrostatic interactions are weak and/or specific sorbent functional groups are present (Du et al., 2014; Li et al., 2021). Some studies also postulated the formation of hierarchical structures of PFAS on various sorbent surfaces (Johnson et al., 2007; Yu et al., 2009), but direct evidence of such structures is largely absent.

78

79

80

81

82

83

84

85

86

87

88

89

90

91

92

93

94

95

96

97

98

99

100

The complexity of PFAS-surface interaction warrants the use of advanced characterization and computational tools to reveal molecular-scale behaviors. For example, Fourier-transform infrared spectroscopy (FTIR) was employed to characterize the surface complexation (Gao and Chorover, 2012; Zhao et al., 2014), ligand exchange (Gao and Chorover, 2012), and hydrophobic interactions (Wei et al., 2017; Zhang et al., 2014) of perfluorooctane sulfonate (PFOS) with various clay minerals. Quartz crystal microbalance with dissipation (QCM-D) is a surface-sensitive mass balance that quantifies the accumulated mass at the surface with a sensitivity of 10 ng/cm<sup>2</sup>. QCM-D has been employed to study the adsorption and conformational changes of proteins on polymers (Nagasawa et al., 2015; Siow et al., 2019) foulants/scalants on membrane functional groups (Huang et al., 2020; Wu et al., 2014), and surfactants on various surfaces (Kou and Xu, 2016; Nalam et al., 2019). To date, only one study has applied OCM-D to investigate PFAS-surface interaction, which showed that PFAS was incorporated into model phospholipid bilayers followed a passive partitioning pathway, and gradually fluidized the bilayer (Fitzgerald et al., 2018). Molecular dynamics (MD) simulations have been used to investigate the interaction of PFAS with clay minerals (Loganathan and Wilson, 2022; Wang et al., 2021; Willemsen and Bourg, 2021; Yan et al., 2020; Yan et al., 2021), polymers (Choudhary et al., 2022; Kancharla et al., 2022), and graphene materials (Jiang et al., 2021). A few studies combined MD simulation with batch sorption experiments (Wang et al., 2021; Yan et al., 2020; Yan et al., 2021). In these studies, the MD simulations for PFAS sorption on clays corroborated the mechanisms suggested by the experimental results and assisted in identifying the PFAS binding sites.

Hydrophobic interaction is a universal mechanism contributing to the sorption of different PFAS on a wide range of sorbents. Therefore, in this study, we employed an integrated approach utilizing QCM-D, atomic force microscope (AFM), and MD simulations to elucidate the hydrophobic interaction between PFAS and surface at the molecular scale. Two model PFASs were employed: perfluorononanoic acid (PFNA) and PFOS, featuring identical lengths of the fluorinated alkyl chain but different head groups (i.e., carboxylate vs. sulfonate). The model hydrophobic surface is a highly ordered, methyl group terminated self-assembled monolayer (CH<sub>3</sub>terminated SAM). QCM-D adsorption measurements of PFAS were first conducted to determine the PFNA/PFOS sorption isotherms and kinetics. The PFAS-adsorbed QCM sensors were then analyzed by AFM imaging and force spectroscopy, which identified the state of the adsorbed PFNA/PFOS molecules on the SAM. Lastly, fully atomistic MD simulations were performed to provide insight into the origins of the PFNA/PFOS molecular behavior at the interface. In our study, we observed higher adsorption of PFNA than PFOS, but the formation of aggregated structures at the hydrophobic surfaces is more predominant for PFOS than for PFNA. This study is among the first to provide a comprehensive mechanistic view of PFAS molecules at the hydrophobic interface.

### 2. Materials and Methods

101

102

103

104

105

106

107

108

109

110

111

112

113

114

115

116

117

118

119

120

121

122

123

## 2.1 Materials and solution preparation

Details on the materials as well as the protocols for preparing solutions and CH<sub>3</sub>-terminated SAM are provided in Supplementary Information (SI) 1. In this study, CH<sub>3</sub>-terminated SAM was

selected as a model hydrophobic surface. Compared with other hydrophobic SAM (e.g., (C<sub>6</sub>H<sub>5</sub>)<sub>n</sub>-SAM), CH<sub>3</sub>-terminated SAMs have fewer gauche defects (Vericat et al., 2005) and thus minimize any confounding effects on the adsorption of PFAS.

## 2.2 QCM-D experiments

124

125

126

127

128

129

130

131

132

133

134

135

136

137

138

139

140

141

142

143

144

145

PFNA/PFOS adsorption experiments were conducted using QCM-D (E4 model, Q-Sense, Biolin Scientific) on CH<sub>3</sub>-terminated SAM-coated sensors at 25 °C with a flow rate of 25 μL min<sup>-</sup> <sup>1</sup>. The changes in frequency ( $\Delta f$ ) and dissipation ( $\Delta D$ ) were recorded across multiple overtones of the sensor's fundamental frequency (5 MHz). Two types of adsorption experiments were conducted: "stepwise" experiments, where the surface was exposed sequentially to a series of PFNA or PFOS solutions (50, 100, 200, 350, and 500 mg/L), were used to determine adsorption isotherm; "single-concentration" experiments, where the sensor was exposed to a single PFNA/PFOS solution, were used to prepare samples for kinetic modeling and AFM analyses. Details are shown in SI 2. The highest PFNA and PFOS concentration used in the experiments (500 mg/L) was below their respective critical micelle concentrations (1299 and 1500 mg/L, respectively (Kunieda and Shinoda, 1976; Reth et al., 2011)). The PFAS solution concentration range was selected to (1) observe measurable mass sorption on the CH<sub>3</sub>-terminated SAM using QCM and (2) mimic the ppm level PFAS concentrations often found near contaminated source sites (Brusseau et al., 2020; Vu and Wu, 2022). The adsorbed masses from the single-concentration experiments were comparable with those from the stepwise experiments (further discussed below). The adsorbed PFNA/PFOS masses were estimated by Sauerbrey's equation and the Kelvin-Voigt model (SI 2). Origin Pro (2022) was used in isotherm and kinetic model fitting.

#### 2.2.1 Adsorption isotherm models

The following isotherm models were evaluated. It should be noted that PFNA/PFOS adsorption did not achieve equilibrium in QCM experiments, even after prolonged exposure (further discussed below). However, this is typical for surfactant adsorption at the interface below CMC (Zeng et al., 2020), and isotherm modeling can still provide mechanistic insight into the molecular behavior at the interface.

(a) The Zhu and Gu adsorption isotherm: This model, initially developed to understand the sorption of sodium dodecyl sulfate (SDS) on polystyrene latex (Zhu and Gu, 1991), involves a two-step process: first, the surfactant molecules are adsorbed individually by interacting with the solid surface; second, enhanced mass accumulation occurs as aggregates (micellar or hemimicellar) form at the interface resulting via interactions with either the free or adsorbed-species. The general form of the model is:

157 
$$m_c = \frac{\left(m_{max} K_1 C\left(\frac{1}{n_g} + K_2 C^{n_g - 1}\right)\right)}{1 + K_1 C(1 + K_2 C^{n_g - 1})} \dots \dots (1)$$

where  $m_c$  (ng/cm<sup>2</sup>) is the amount of adsorbate on the surface at equilibrium when the surfactant concentration is C (mg/L);  $m_{max}$  (ng/cm<sup>2</sup>) is the theoretical maximum adsorption capacity;  $K_1$  (L/mg) and  $K_2$  (L/mg)<sup>ng-1</sup> are the equilibrium constants of the reaction between the surface and the surfactant molecules (first step) and that between the adsorbed surfactants from the first step and incoming surfactant molecules (second step); and  $n_g$  is the aggregation number. In this study, two limiting cases of Equation (1) are considered:

(i) When  $K_2 \to 0$  and  $n_g \to 1$ , Equation (1) reduces to the Langmuir isotherm equation (Langmuir, 1918), which describes the monolayer surface coverage of the adsorbate on a

homogeneous adsorbent and assumes no interactions among the molecules in the solution or after adsorption on the surface:

$$m_c = \frac{\left(m_{max,L} K_L C\right)}{1 + K_L C} \dots \dots (2)$$

where and  $K_L$  (L/mg) is the Langmuir adsorption constant.

170 (ii) When  $K_2C^{n-1} \gg 1$  or  $K_1C \ll 1$ , Equation (1) reduces to

171 
$$m_c = \frac{m_{max,G} K_G C^{n_g}}{1 + (K_G C^{n_g})} \dots \dots (3)$$

where  $K_G$  (L/mg)<sup>ng</sup> is the product of  $K_1$  and  $K_2$ . This form, henceforth called "Zhu and Gu aggregate-type isotherm", has been used in the literature to describe the sorption and subsequent aggregation of surfactants SDS on *Moringa oleifera* seed extract (Beltran-Heredia and Sanchez-Martin, 2009), pentaethylene glycol monodecyl ether on silica (Thibaut et al., 2000), and Marolophen NP5 on ultrafiltration membranes (Nguyen et al., 2015).

(b) Freundlich isotherm: This model describes the sorption behavior for a heterogeneous surface and/or multilayer adsorption of the adsorbate (Freundlich, 1907).

180 
$$m_c = K_F * C^{\frac{1}{n_f}} \dots \dots (4)$$

where  $K_F(\text{ng cm}^{-2} \text{L}^{1/\text{n}_f} \text{mg}^{-1/\text{n}_f})$  is the Freundlich distribution constant; and  $1/n_f$  (dimensionless) is the degree of heterogeneity. In this equation,  $1/n_f > 1$  represents cooperative sorbate-sorbate interactions.

## 2.2.2 Adsorption kinetic model

The time profiles of  $\Delta m$  for PFNA/PFOS adsorption were fit to the Avrami kinetic model (Avrami, 1939; 1940; 1941). Originally developed to model the kinetics of phase change during crystallization, this sigmoidal model has later been used to describe the sorption of heavy metals (Lopes et al., 2003; Zheng et al., 2021), dyes (Cestari et al., 2005; Royer et al., 2009; Vargas et al., 2011), and organic micropollutants (Djilani et al., 2012).

190 
$$\frac{m_t - m_0}{m_{max} - m_0} = 1 - \exp(-k_{av} * t^{n_{av}}) \dots \dots (5)$$

where  $m_0$  (ng/cm<sup>2</sup>) is the initial amount of adsorbate on the surface;  $k_{av}$  (min<sup>-nav</sup>) is the

Avrami kinetic constant;  $n_{av}$  is a constant related to the adsorption order, and t (min) the time.

The linearized form of this equation is presented as:

$$ln{-\ln(1-\alpha)} = n_{av} \ln t + \ln k_{av} \dots \dots (6)$$

where  $\alpha$  is the left-hand side of Equation (6). This form of the Avrami kinetic model enables the identification of different rates of physicochemical processes occurring during the sorption process (Cestari et al., 2004; Vieira et al., 2007).

## 2.3 AFM imaging and force mapping

AFM imaging and force mapping (BioInfinity, Oxford Instrument, USA) were employed to characterize the bare gold QCM sensors, CH<sub>3</sub>-terminated SAM, and PFNA/PFOS-adsorbed surfaces. AFM measurements were performed within 72 h after QCM experiments. The samples were equilibrated in DI water for at least 30 min prior to data acquisition to minimize thermal drift.

Topographical images of the CH<sub>3</sub>-terminated SAM with adsorbed PFNA/PFOS were obtained using tapping (silicon cantilever,  $k_n \sim 42$  N/m) and/or contact (silicon cantilever,  $k_n \sim 0.2$ 

N/m) imaging modes. The average root-mean-square roughness ( $R_q$ ) for the samples was obtained from measuring on at least three locations, each with a scan area of 500 nm  $\times$  500 nm.

For force mapping, an AFM cantilever with a sharp silicon nitride tip ( $k_n \sim 0.02$  N/m and tip radius  $\sim 20$ -30 nm) was employed. The stiffness of the cantilever was calibrated using the thermal noise method (Butt and Jaschke, 1995); the deflection sensitivity of the cantilever was measured by obtaining a force-distance profile on freshly cleaned silicon dioxide surfaces in DI water. For each sample, six force maps (144 force-distance (FD) curves per map) were obtained at random locations, each with a scan area of 500 nm  $\times$  500 nm and a trigger force of 5 nN. The approach velocity of the cantilever was held at 250 nm/s to minimize the effects of hydrodynamic forces on the force measurements. This approach velocity was kept constant across all experiments.

# 2.4 Molecular dynamics simulations

Fully atomistic MD simulations were performed. A gold substrate of a dimension of 40 × 40 × 10 ų with the top surface orientation as (111) was fixed as a rigid body. The surface of the gold substrate was passivated with a layer of SAM molecules. Initially, 24 identical PFNA/PFOS molecules were vertically suspended above the SAM layer, corresponding to a surface coverage of 1.5 molecules/nm² of the adsorbed PFNA/PFOS masses (142–421 ng/cm², equivalent to 1.7–5.4 molecules/nm²) obtained from QCM-D experiments (500 mg/L PFNA/PFOS, 2h). The timestep in our simulations is 0.1 femtosecond; 20 million timesteps were calculated for each simulation. Separate simulations were conducted to evaluate the effects of the initial orientation of the PFNA/PFOS molecules: tail-up (i.e., C-F tail pointing away from the SAM interface) or tail-down. An equilibration is held until the molecules fully interact with the surface and the total energy of the system and the position of molecules have reached to a stabilized condition. Since

we focus on the near-surface interaction between PFNA/PFOS and CH<sub>3</sub>-terminated SAM, no water molecules were considered in the simulation. The simulations have periodic boundary conditions in both the *x*- and *y*-axis. A Langevin thermostat was applied to the free atoms to maintain a temperature equilibrium of 300 K. The inter-atomic interactions among the SAM molecules and PFNA/PFOS were described via the optimized potentials for the liquid simulations (OPLS) force field. The simulations (Jorgensen et al., 1996; Jorgensen and Tirado-Rives, 1988) were performed using LAMMPS software (Plimpton, 1995; Thompson et al., 2022). The density of atoms in the *z*-axis is calculated as the total number of atoms per bin in the *z*-direction.

## 3. Results and Discussion

# 3.1 Adsorption of PFNA and PFOS in QCM-D experiments

The synthesized CH<sub>3</sub>-terminated SAM has similar characteristics as those reported in the literature (Huang et al., 2020; Zhang et al., 2017) (SI 3). The sorption of PFNA/PFOS on SAM in QCM experiments is shown in Figure 1 (stepwise experiments). The frequency drops indicate added PFNA/PFOS mass on the CH<sub>3</sub>-terminated SAM (Nalam et al., 2019). As solution concentration increased, the frequency drop became greater. There was negligible change in dissipation at low PFNA/PFOS concentrations, but dissipation increased when PFNA/PFOS concentrations increased above 100 mg/L. A preliminary experiment using PFNA suggests that the adsorption process did not achieve equilibrium even after exposure up to 20 h (Figure S2); however, a rapid frequency drop occurred within the first 30 min after the PFAS solution was introduced to the surface, followed by a significantly slower mass change with time. Therefore, a 2 h interval was employed in all stepwise experiments as the adsorption period at each solution concentration to capture the initial interactions between PFNA/PFOS and the CH<sub>3</sub>-terminated SAM. At the same solution concentration, the frequency drop was greater in PFNA experiments

than in PFOS experiments, suggesting higher PFNA adsorption at the hydrophobic surface (assuming either insignificant or comparable trapped solvent by both PFAS). For example,  $\Delta f$  at the end of the 2h adsorption was -4.1 ± 2 Hz (three replicates) and -2.2 ± 2 Hz for 50 mg/L PFNA and PFOS, respectively. After solvent rinse, the magnitude of  $\Delta f$  decreased by 2-10 Hz (Figure S3), indicating that a fraction of the adsorbed PFNA/PFOS molecules were weakly associated with the surface and were rinsed away.

The adsorbed masses for PFNA and PFOS were calculated using Sauerbrey's equation ( $\leq$  100 mg/L) and Kelvin-Voigt's model (200-500 mg/L), respectively, because when PFNA/PFOS solution concentrations exceeded 100 mg/L,  $\Delta f$  values varied with overtone and  $\Delta D$  exceeded  $1\times10^{-6}$ , indicating a viscoelastic nature of the adsorbed layers. The accumulated adsorbed mass (before rinse) at each solution concentration is shown in Table S1. More PFNA mass/molecules are adsorbed than PFOS. For example, after 2 h exposure to 200 mg/L solution, the adsorbed PFNA mass ( $226 \pm 19 \text{ ng/cm}^2$ ;  $486 \pm 41 \text{ pmol/cm}^2$ ) is greater than that of PFOS ( $127 \pm 30 \text{ ng/cm}^2$ ;  $254 \pm 60 \text{ pmol/cm}^2$ ).

A comparison of the adsorbed PFNA/PFOS mass between stepwise and single-concentration experiments at the same adsorption time (2 h) did not show a significant difference (Figure S4), suggesting that the adsorption history did not substantially impact the adsorption behavior (Nalam et al., 2019). Correspondingly, the adsorbed masses from the stepwise experiments were used for isotherm modeling.

Three isotherm models were evaluated. The Freundlich model showed the most inferior fit, while the Langmuir (Equation 2) and Zhu and Gu aggregate-type (Equation 3) isotherms were comparable (Figure 2 and Table 1). However, true Langmuir adsorption is unlikely for PFNA/PFOS at the interface, given the absence of an equilibrated mass even after 20 hours (Figure

S2b) and based on the AFM characterization results below. On the other hand, the  $n_g$  values in the Zhu and Gu aggregate-type model were greater than 1 for both PFNA and PFOS, indicating a possible association among the adsorbed molecules on the surface.

274

275

276

277

278

279

280

281

282

283

284

285

286

287

288

289

290

291

292

293

294

295

296

Figure 3a shows the initial adsorption kinetics of PFNA and PFOS (at 50 mg/L and 500 mg/L) on CH<sub>3</sub>-terminated SAM, all exhibiting an "S-shaped" profile. The pseudo first- or secondorder kinetic models previously used in PFAS batch sorption studies (Askeland et al., 2020; Wei et al., 2017) did not fit our data. Because the first 20 min adsorption accounted for > 90% of the total mass adsorbed (Figure S5), the corresponding data were used for fitting to the linearized Avrami kinetic model (Figure 3b). For all four fittings, two distinct segments were observed, suggesting that there were different dominant interaction mechanisms as the adsorption progresses over time (Cestari et al., 2004; Vieira et al., 2007). The kinetic fitting parameters for the two segments are presented in Table 2. For the first segment, the  $n_{avl}$  values for PFNA and PFOS are similar and exhibit similar concentration dependence. This allows  $k_{avI}$  values between PFNA and PFOS to be compared (given the similar units min<sup>-nav</sup>). The similar  $n_{avl}$  and  $k_{avl}$  values suggest that PFNA and PFOS behaved similarly at this initial adsorption stage; the PFNA/PFOS molecules mostly likely interacted with the SAM surface directly. The transition into the second segment occurred at ~11 min (ln  $t \approx 2.4$ ). The difference in  $n_{av2}$  values between PFNA and PFOS suggests that their adsorption mechanisms started to diverge, possibly involving different degrees of lateral diffusion and aggregation after the surface became more "crowded" with the adsorbed PFAS as suggested by AFM and MD analyses below.

In summary, the QCM experiments show that PFNA shows higher adsorption capacity on CH<sub>3</sub>-terminated SAM than PFOS. The adsorption isotherm and kinetic modeling suggest that there is likely a range of PFNA and PFOS behaviors at the interface.

#### 3.2 AFM characterization of surface-adsorbed PFNA and PFOS

Figure 4 shows that, after PFNA/PFOS adsorption, the underlying SAM features were retained, but a few globular structures of 15–35 nm in width were also observed. The section profiles show that these structures are 5-8 nm in height. Considering that these structures have dimensions more than double the length of PFNA/PFOS molecules ( $\sim$ 1.14 nm) (Torres et al., 2009; Wang et al., 2015), they should be aggregates or hierarchical structures of PFNA/PFOS molecules. The globular structures were predominantly found near the grain boundaries, indicating that surface roughness as low as  $1.26 \pm 0.10$  nm can possibly assist the initiation of PFAS molecule aggregation.

Although visually distinct on the AFM images, the globular structures do not account for the majority of the adsorbed PFNA/PFOS mass based on this estimate: using the molar volume of PFNA 264.7 cm³/mol and assuming the globular features in Figure 4b are spherical PFNA micelles with an average diameter of 10 nm and the highest possible packing density (i.e., the same density as a pure PFNA phase), the 9 micelles on the 0.25 µm² surface captured by the image contributes to only 3.3 ng/cm² PFNA, less than 1% of the total PFNA mass adsorbed (494 ng/cm²). In other words, most PFNA/PFOS molecules adsorbed as thin molecular layer(s) not resolved via AFM images, possibly lying parallel on the surface due to dominating hydrophobic interactions.

AFM force mapping was conducted to further characterize the structural organization of PFNA/PFOS on CH<sub>3</sub>-terminated SAM surfaces. First, pull-off forces from the retract FD curves were determined from three force maps collected at random locations on the sample (Figure 5). The pull-off forces for the PFNA- and PFOS-adsorbed surfaces (0.75  $\pm$  0.34 and 1.0  $\pm$  0.20 nN, respectively) are 3-4 times higher than that for CH<sub>3</sub>-terminated SAM (0.23  $\pm$  0.03 nN). The higher

adhesion forces can be attributed to the greater hydrophobic interaction of the silica tip with the CF<sub>3</sub> groups in PFNA/PFOS than that with the CH<sub>3</sub> terminal groups on the SAM surface. Additionally, the PFNA/PFOS-adsorbed SAMs showed a greater spread in the pull-off forces than the fresh SAM surface, suggesting different orientations, densities, and/or structures of PFNA/PFOS molecules at the hydrophobic interface.

319

320

321

322

323

324

325

326

327

328

329

330

331

332

333

334

335

336

337

338

339

340

341

Second, the approach FD curves from six force maps were examined for PFNA/PFOSadsorbed surfaces. A portion of these approach curves showed one or more discontinuities ("force steps"), i.e., a drop in the force as the separation distance between the approaching tip and the surface is decreased. The characteristic features of force steps are as defined in Figure 6a. A force step arises when the AFM tip initially compresses a stiff hierarchical structure or an aggregate adsorbed at the interface during approach and, upon reaching a contact force higher than the stiffness of the structure, ruptures the structure and squeezes out of the confinement between the tip and substrate. Because the interface in our measurements is a compressible SAM layer (instead of a hard silica substrate), the zero separation between the structure/aggregate and the SAM interface is set at the base of the slope closest to the infinite wall (the grey portion in Figure 6a is dominated by the compression of the SAM layer). A higher percentage of the approach curves for the PFOS-adsorbed surface (39%) displayed force steps in comparison with those for the PFNAadsorbed surface (6%), indicating that PFOS molecules are more likely to form aggregates/structures despite fewer adsorbed molecules. A consistent trend was observed in triplicate samples.

The characteristics of the force steps indicate the type and nature of the aggregate/structure. For example, FD curves with two consecutive force steps may represent an ordered structure with two layers, usually observed for micelles or bilayers. The distribution of step size, slope, and

distance from the interface for all FD curves with force steps is shown as histograms in Figures 6b-d. Figures 6e and 6f explore the relationship between the stiffness, the distance from the SAM interface, and the size of the aggregates/structures. There is no correlation between the stiffness and the distance of the PFNA/PFOS aggregates/structures from the SAM interface, but most aggregate/structures are 1–5 nm in size. The majority of the PFNA aggregates/structures were soft (slope < 0.2 N/m), formed at the vicinity of the SAM interface ( $x_l = 0$ ), and their FD curves presented only one force step. In comparison, most PFOS aggregates/structures were also soft, but a much higher number of their FD curves displayed multiple force steps, with some features considerably far away from the SAM interface. FD curves with 1–3 force steps within 10 nm from the interface likely correspond to hierarchically layered or micellar structures of PFOS molecules, but the those with force steps more than 10 nm away are unlikely to originate from multi-layered, densely-packed structures. Further inspection of these FD curves showed that they exhibit a distinct plateau in force between the force steps (example shown in the inset of Figure 6d), a unique feature previously reported for the FD curves resulting from the presence of air bubbles on graphite (Wang et al., 2017). This plateau corresponds to a process where the AFM tip presses onto the air bubble (Walczyk and Schonherr, 2014; Wang et al., 2017). Indeed, careful topographic and phase imaging (soft-tapping) of PFOS-adsorbed surfaces showed spherical structures with dimensions larger than 20 nm, indicating the formation of stabilized air bubbles at the hydrophobic interface (SI 10). PFASs are known to partition at the air-water interface (Liu et al., 2022; Lyu et al., 2018; Meng et al., 2014). Notably, air bubble-assisted sorption was found to contribute to more than 70% of PFOS sorption on carbon nanotubes and graphene (Meng et al., 2014). Given the absence of nanobubbles on PFNA-adsorbed SAM surfaces, the nanobubbles on the PFOS-adsorbed surfaces likely originated from the solution where PFOS molecules stabilized the trapped air.

342

343

344

345

346

347

348

349

350

351

352

353

354

355

356

357

358

359

360

361

362

363

Collectively, the AFM imaging and force mapping revealed the state of the PFNA/PFOS molecules adsorbed on the CH<sub>3</sub>-terminated SAM: while a small fraction of molecules formed large aggregates, others lay flat or formed small aggregates or hierarchical structures. This indicates a non-negligible heterogeneity in the PFNA/PFOS adsorption behavior despite the relatively homogeneous hydrophobic surface.

# 3.3 Molecular dynamics simulations

MD simulations were employed to further elucidate the molecular interactions of PFAS at the hydrophobic SAM interface. The CH<sub>3</sub>-terminated SAM constructed on the gold substrate (40 × 40 Å<sup>2</sup>) was brought in contact with 24 molecules of either PFNA or PFOS to match the range of the surface coverage of the adsorbed molecules obtained from the QCM adsorption experiments. Two initial orientations of the PFNA/PFOS molecules were evaluated, *i.e.*, all the molecules were brought towards the surface with either tail-up (fluorocarbon chain away from SAM surface) or tail-down configurations. All simulations reached equilibrium by the end of the simulation, as shown by the total energy (Figure S8) and radial distribution function at different times (Figure S9). The system achieved equilibrium faster when PFNA/PFOS molecules were initially in the tail-down orientation, as expected from the greater affinity of the fluorocarbon chain than the polar head group towards the hydrophobic SAM.

Figures 7a-d show the top-view molecular snapshots and the corresponding 2D (*xy plane*) density maps of PFNA and PFOS molecules adsorbed on the CH<sub>3</sub>-terminated SAM (with tail-down initial orientation). The top-view snapshots show that PFOS molecules on the surface are more likely to have their head groups pointing away from the surface and avoiding the hydrophobic SAM interface (Figure 7b), while the PFNA molecules largely lay flat (Figure 7a), maximizing the interactions between the fluorocarbon chain and the SAM interface. Moreover, the 2D density

profile of PFNA molecules (Figure 7c) displayed a greater uniformity in atomic density than PFOS (Figure 7d), suggesting that PFNA molecules resulted in a more homogenous coverage, while PFOS molecules tend to form aggregates, consistent with the results from the AFM force measurements. The greater degree of aggregation of PFOS than PFNA at the SAM interface was also observed when the initial PFNA/PFOS orientation was tail-up (SI video V1\_tail-up). The 1D density profiles (figure 7f) for adsorbed PFNA or PFOS showed that the maximum density (peak position) for PFOS was farther away than that for PFNA from the SAM interface. The preferential interactions of PFOS molecules with each other rather than with SAM suggests the higher probability for PFOS molecules to form aggregated structures. In comparison, PFNA's preferential interaction with the CH<sub>3</sub>-terminated SAM can explain the greater PFNA adsorption, consistent with OCM results.

The simulation also revealed an additional interaction between PFNA/PFOS molecules and the CH<sub>3</sub>-termianted SAM. As shown in the side-view snapshots (Figure 7e), some fluorocarbon chains of the PFNA and PFOS molecules insert into the SAM layer. The *z*-direction density profiles of atoms (Figure 7f) showed there exists a more significant overlap in the density profiles between PFNA and SAM than between PFOS and SAM, indicating more PFNA molecules inserted into SAM. The insertion behavior of PFNA molecules into SAM may impact their lateral diffusion and reduce the tendency to form aggregated structures at the interface.

# 3.4 Comparing molecular-scale and macro-scale PFAS sorption studies

Our study used a model hydrophobic surface, CH<sub>3</sub>-terminated SAM, to isolate the hydrophobic interaction as a PFAS sorption mechanism. The molecular-level characterization of PFAS adsorption in this study revealed some different phenomena compared with those obtained

from batch experiments. For example, in contrast to the greater PFNA adsorption in our experiments, PFOS is adsorbed more than PFNA in soil ( $log K_d$  of PFOS ~1.5-1.8 times greater) (Nguyen et al., 2020; Pereira et al., 2018), attributable to a combination of different mechanisms other than hydrophobic interaction (e.g., electrostatic interactions) (Cai et al., 2022). The S-shaped Avrami adsorption kinetics observed in our experiments is distinct from previous studies, which used the biexponential model indicative of two (or more) types of sorption sites (e.g., PFOS sorption on natural soil (Li et al., 2019), sediment (Higgins and Luthy, 2006), chitosan (Zhang et al., 2011), and sewage sludge (Zhang et al., 2013)) or used the pseudo-second-order model reflective of PFAS-sorbent chemical interaction (e.g., PFOS sorption on soils (Askeland et al., 2020; Wei et al., 2017), montmorillonite clay (Zhou et al., 2010), and activated carbon and anion exchange resin (Deng et al., 2015; Yu et al., 2009)). By directly measuring adsorbed mass using QCM with high temporal resolution and nanogram-level sensitivity, we were able to capture the S-shaped Avrami kinetics revealing the evolution of adsorption mechanisms over time. Although Langmuir and Zhu and Gu aggregate-type models fit the adsorption data comparably, the AFM and MD analyses clearly showed the presence of hierarchical structure and/or aggregates of PFNA/PFOS molecules on SAM surface and the possible insertion of their fluorocarbon tail into the hydrophobic layer, both violating the Langmuir isotherm assumption of homogeneous adsorption. The diverse PFAS molecular behavior at the interface, despite the homogeneity of SAM, suggests that systematic evaluation is needed to establish the fate of these molecules.

#### 4. Conclusion

410

411

412

413

414

415

416

417

418

419

420

421

422

423

424

425

426

427

428

429

430

431

432

This study integrated QCM-D, AFM (imaging and force spectroscopy), and MD simulations to probe the fundamental mechanisms of PFAS sorption at the hydrophobic interface.

On CH3-terminated SAM, a relatively homogeneous model hydrophobic surface, a range of PFAS

molecular behavior was observed. Adsorbed PFNA/PFOS molecules generally lie flat or form small aggregate/hierarchical structures on the surface, while a small fraction of them forms large aggregates or, in the case of PFOS, associate with nanosized air bubbles at the interface. A comparison of PFNA and PFOS revealed the impacts of the head group polarity. PFNA with the carboxylate head group is adsorbed more than PFOS with the sulfonate head group; however, a greater percentage of adsorbed PFOS molecules forms aggregates/hierarchical structures. Both PFNA and PFOS showed multistage adsorption kinetics, consistent with a sorption process involving an initial interaction between SAM and the PFNA/PFOS molecules and the subsequent lateral diffusion of adsorbed PFNA/PFOS molecules to form aggregates. PFNA and, to a lesser extent, PFOS can insert into the CH<sub>3</sub>-terminated SAM layer, which is consistent with the greater tendency of PFNA to be adsorbed and its more uniform distribution at the interface. Considering that hydrophobic interaction is a universal sorption mechanism for a wide range of PFAS and surfaces, our results contribute to the understanding of PFAS sorption by natural and engineered sorbents (e.g., through interaction with the organic fraction of soil/sediment and the polymer backbone of resins), especially regarding to the molecular behavior near sorption sites where PFAS molecules are enriched.

449

450

451

452

433

434

435

436

437

438

439

440

441

442

443

444

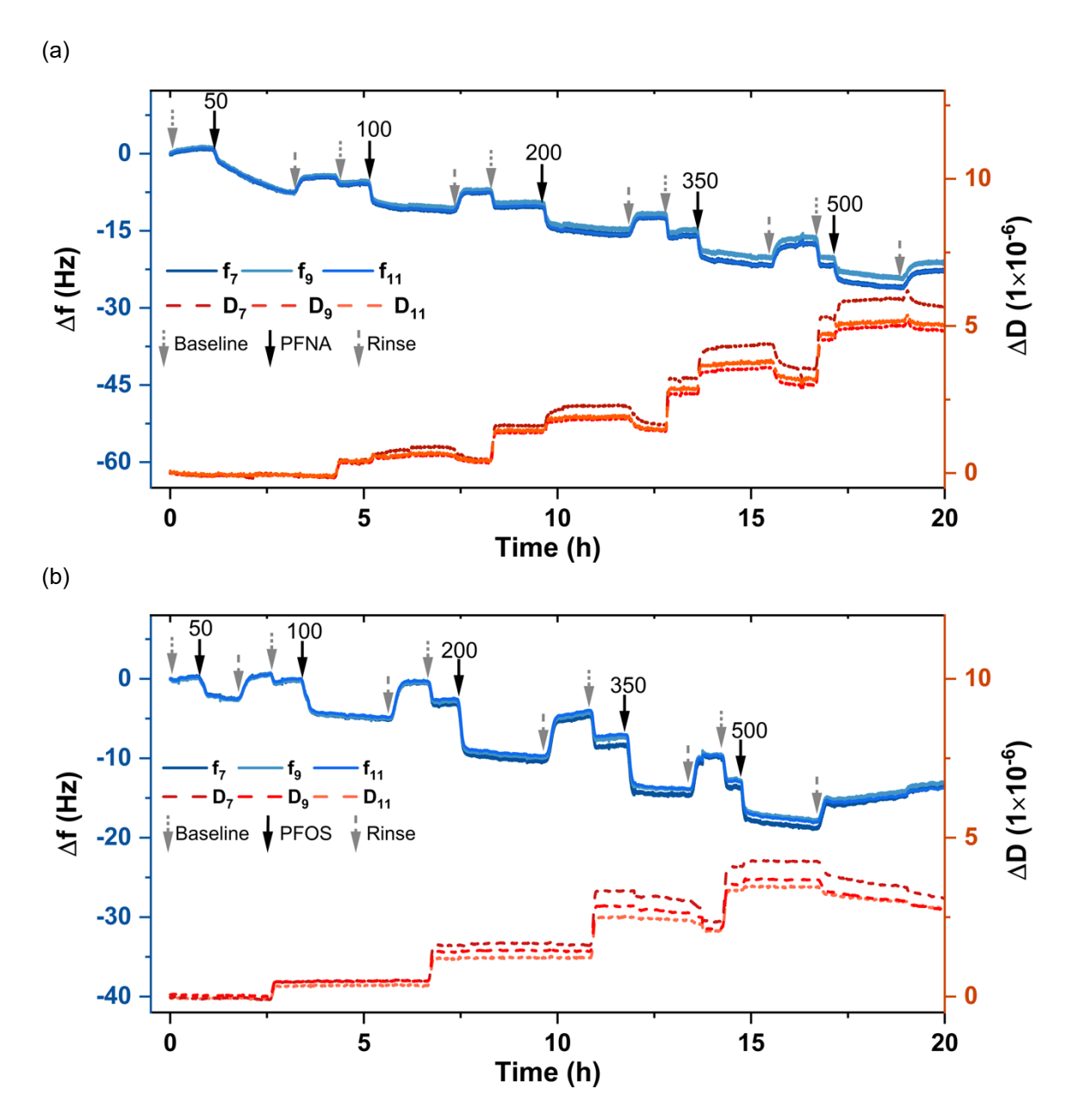
445

446

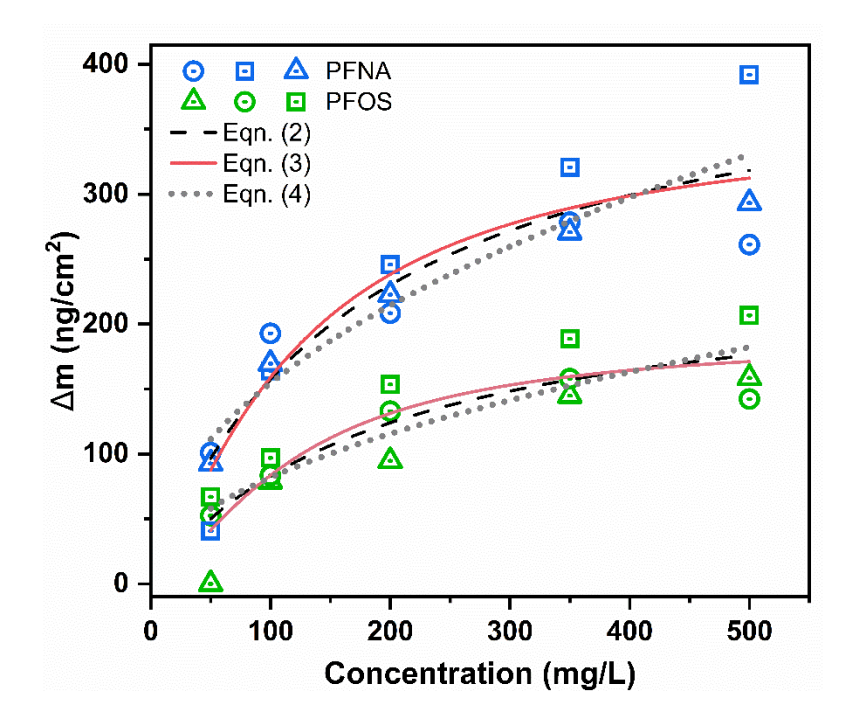
447

448

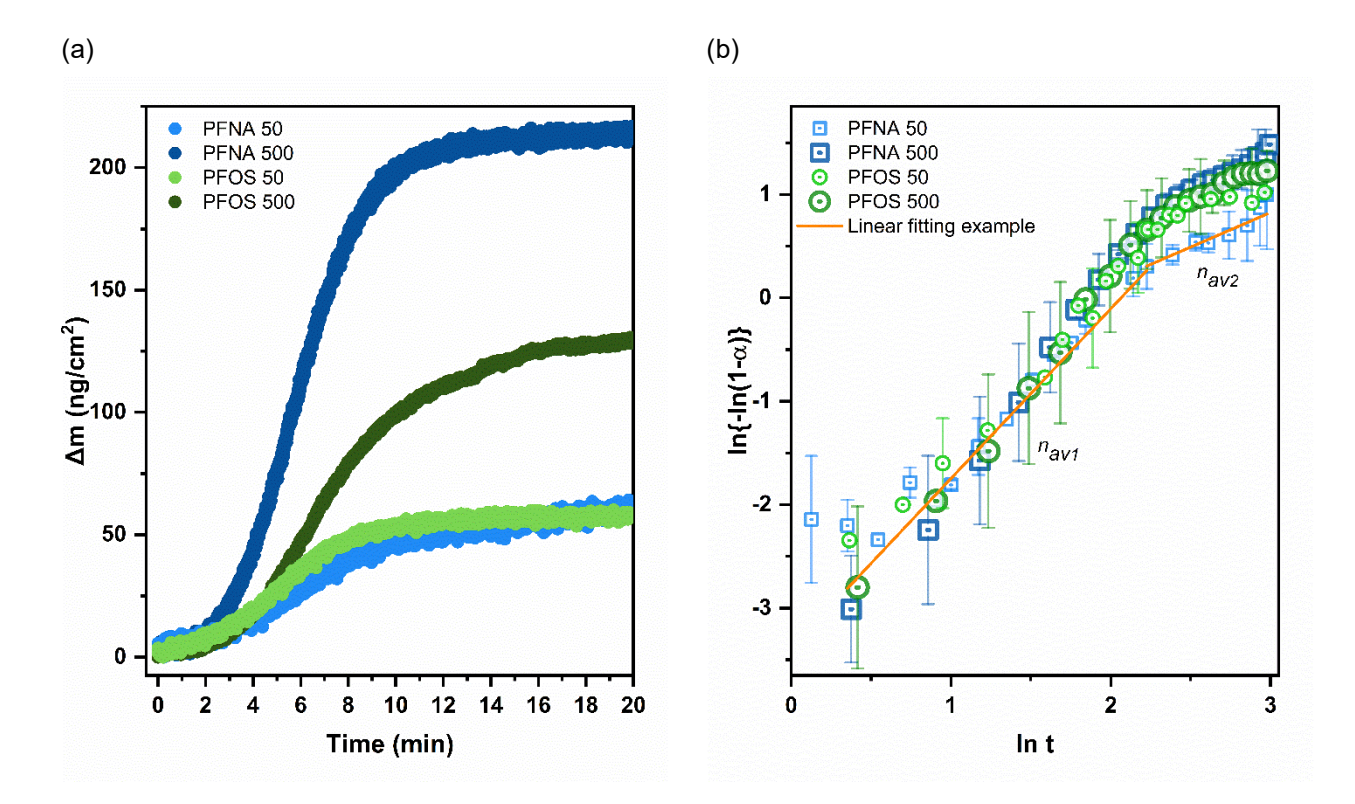
**Acknowledgement:** This work was partially supported by the National Science Foundation (OISE #2230728) and the Mark Diamond Research Fund of the Graduate Student Association at the University at Buffalo, The State University of New York.



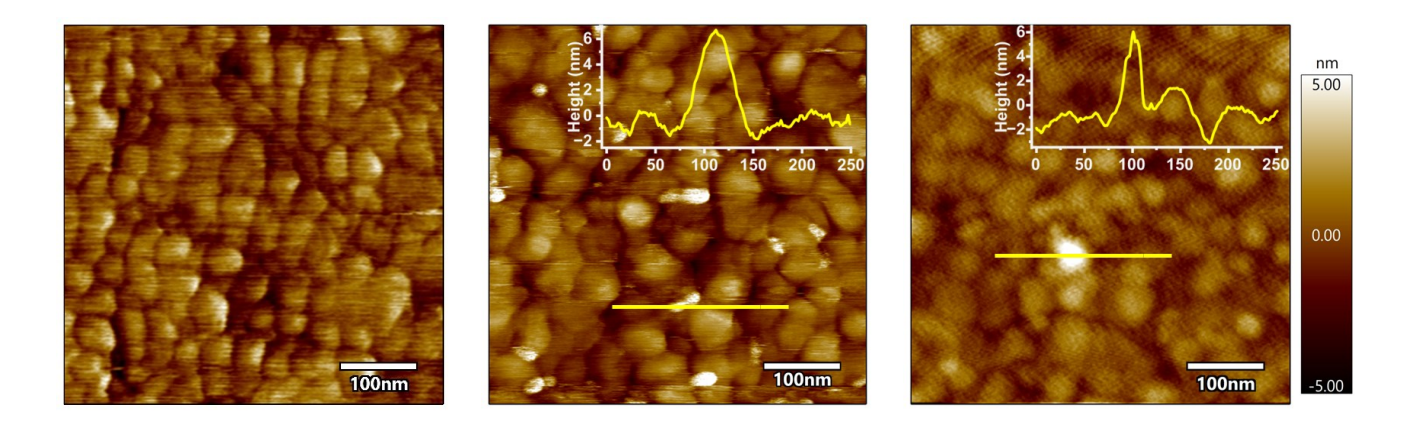
**Figure 1.** Changes in frequency ( $\Delta f$ ) (left axis) and dissipation ( $\Delta D$ ) (right axis) at the 7<sup>th</sup>, 9<sup>th</sup>, and 11<sup>th</sup> overtones for (a) PFNA and (b) PFOS adsorption on CH<sub>3</sub>-terminated SAM. The baseline and rinse solutions before and after each adsorption have the same solvent composition as the corresponding PFAS solution (see SI 1 and 2 for details).



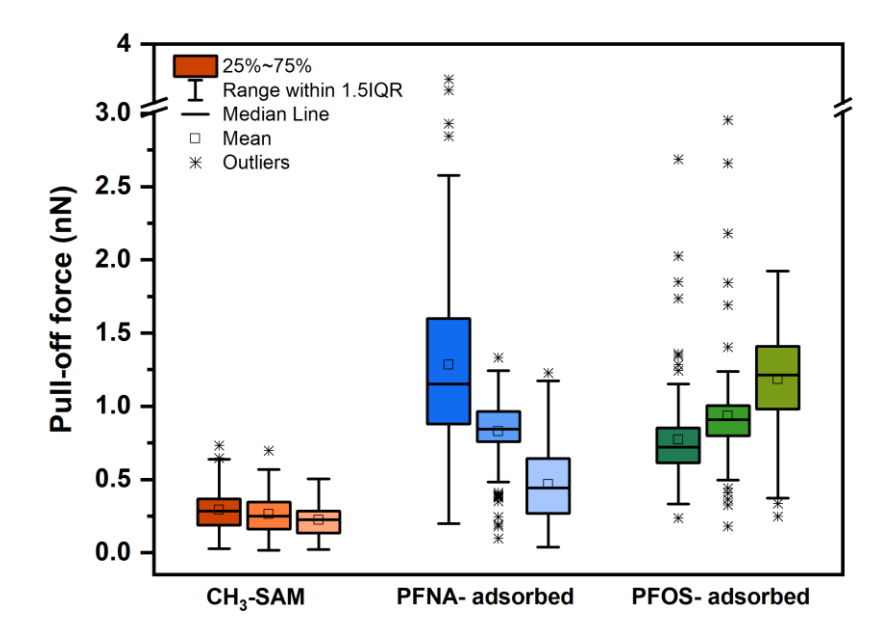
**Figure 2.** Adsorbed mass of PFNA and PFOS (before rinse) from stepwise QCM adsorption experiments and the fitting to three isotherm models. Symbols of different shapes represent the data obtained from replicate experiments. The QCM experimental conditions are as described in Figure 1 caption and in section 2.2. Isotherm fitting parameters are shown in Table 1. The mass data are shown in Table S1.



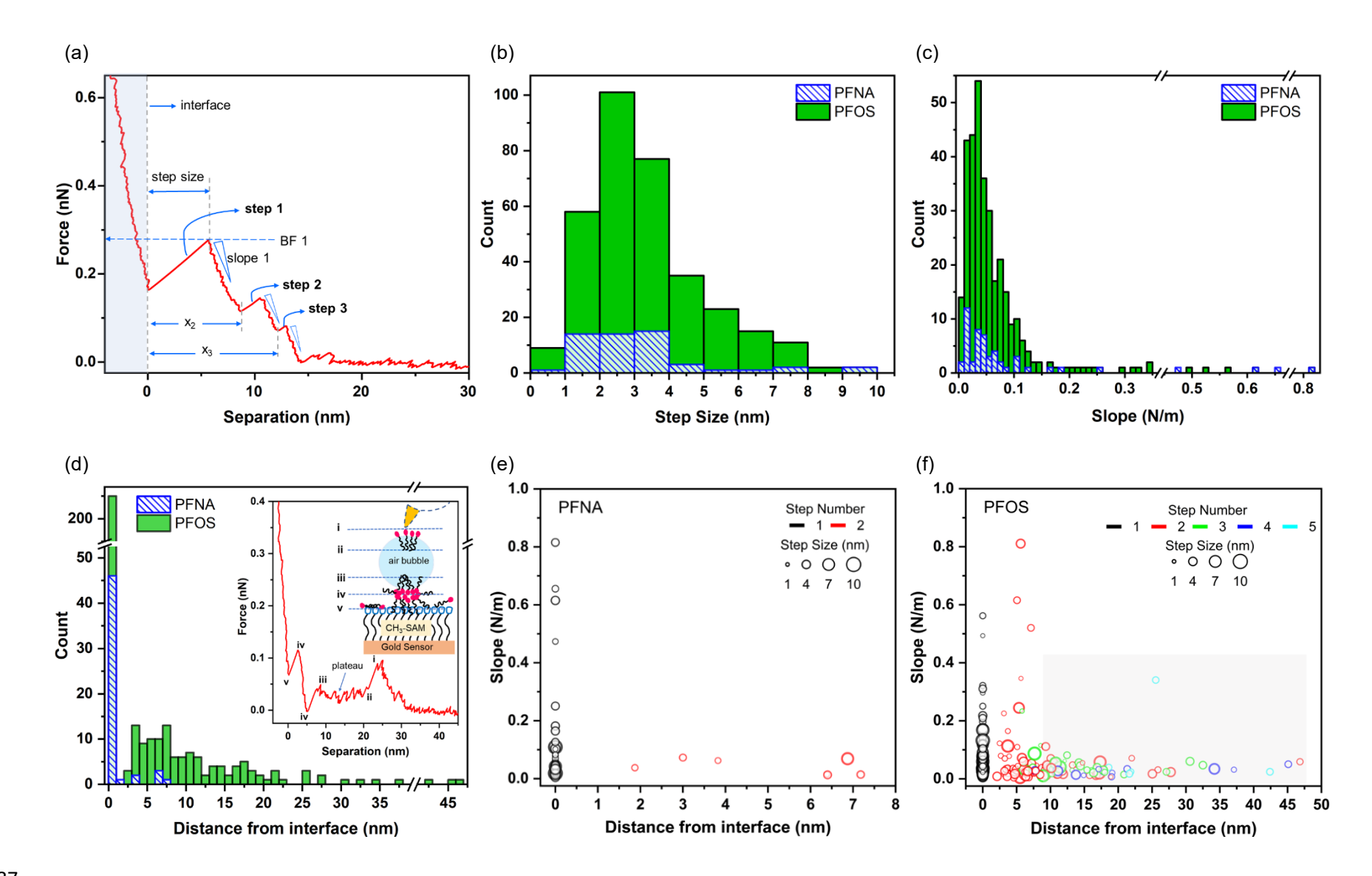
**Figure 3. (a)** Representative mass accumulation profiles of PFNA and PFOS during the first 20 min of adsorption for solution concentrations at 50 mg/L and 500 mg/L. (b) Fitting to the linearized Avrami model. Example fitting lines are shown for the PFNA adsorption data at 50 mg/L solution concentration. The fitting parameters are shown in Table 2. Data are from single-concentration experiments. Error bars in (b) are from the average of triplicate experiments.



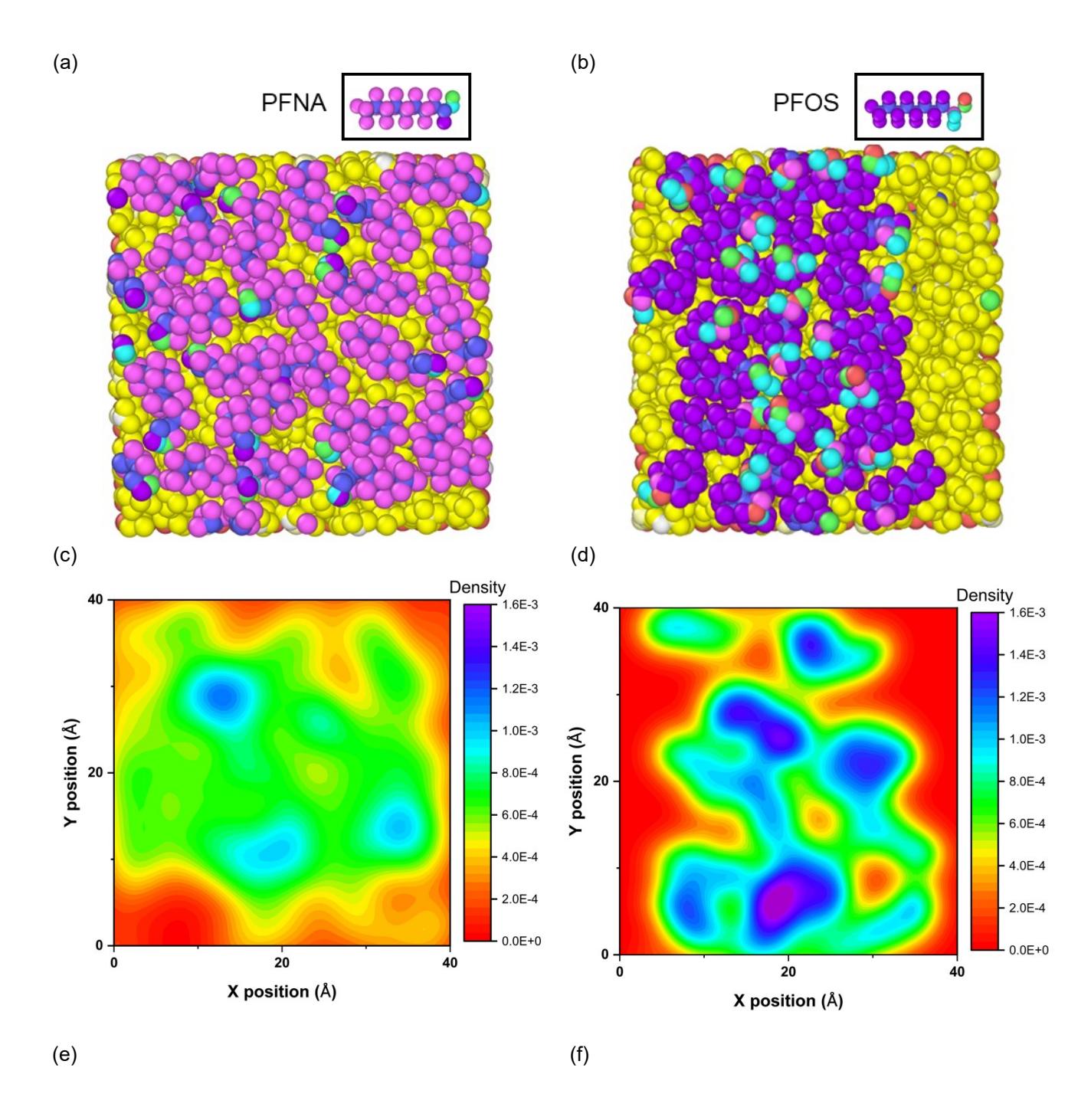
**Figure 4.** Representative AFM images of CH<sub>3</sub>-terminated SAM (a) as freshly prepared and after adsorption of (b) PFNA or (c) PFOS in QCM-D experiments. The insets in (b) and (c) show the section profile of the hierarchical structures. Samples for (b) and (c) were from QCM single-concentration experiments (500 mg/L, 12 h exposure and no rinse); the final adsorbed PFNA and PFOS masses were 494 and 354 ng/cm<sup>2</sup>, respectively.



**Figure 5.** Box-whisker plots of the pull-off forces between the AFM silica tip and CH<sub>3</sub>-terminated, PFNA-adsorbed and PFOS-adsorbed SAMs are presented. PFNA/PFOS-adsorbed samples were obtained from single-concentration QCM experiment with 500 mg/L solution concentration, 12 h exposure, no rinse. The different shades represent the FD measurements at three different locations on each sample (432 FD curves per sample). The force measurements were taken in DI water. The histograms of the pull-off forces are shown in Figure S6.



**Figure 6.** (a) A representative approach curve in the FD curve resolving the hierarchical structures/aggregates of PFNA/PFOS adsorbed on CH<sub>3</sub>-terminated SAM. Zero separation (interface) is set at the base of the step closest to the infinite wall as the top interface of the CH<sub>3</sub>-terminated SAM. The grey-shaded region in (a) represents the compression of the CH<sub>3</sub>-terminated SAM. The following force step characteristics are as defined in (a): step size (horizontal distance of the force step), step number (i=1 is the step closest to the SAM surface), the distance of each force step from the SAM interface ( $x_i$ ), breakthrough force (maximum force before the rupture of the aggregate), and the corresponding slope (stiffness of the structure). The histograms show the distribution of (b) step size, (c) slope, and (d) distance from interface for the force steps obtained from approaching FD curves. Inset in (d) shows a representative FD curve for PFOS-adsorbed surface featuring steps at large distance from interface (> 10 nm), indicative of interaction between the AFM tip and PFOS molecules adsorbed on a nanosized air bubble. The relationship between the stiffness of the aggregates vs. their distance from the interface is explored in (e) and (f) for PFNA- and PFOS-adsorbed surfaces, respectively. The diameter of the circle symbols is proportional to the step size. For each sample, 864 FD curves were obtained from the force maps measured at 6 random locations.



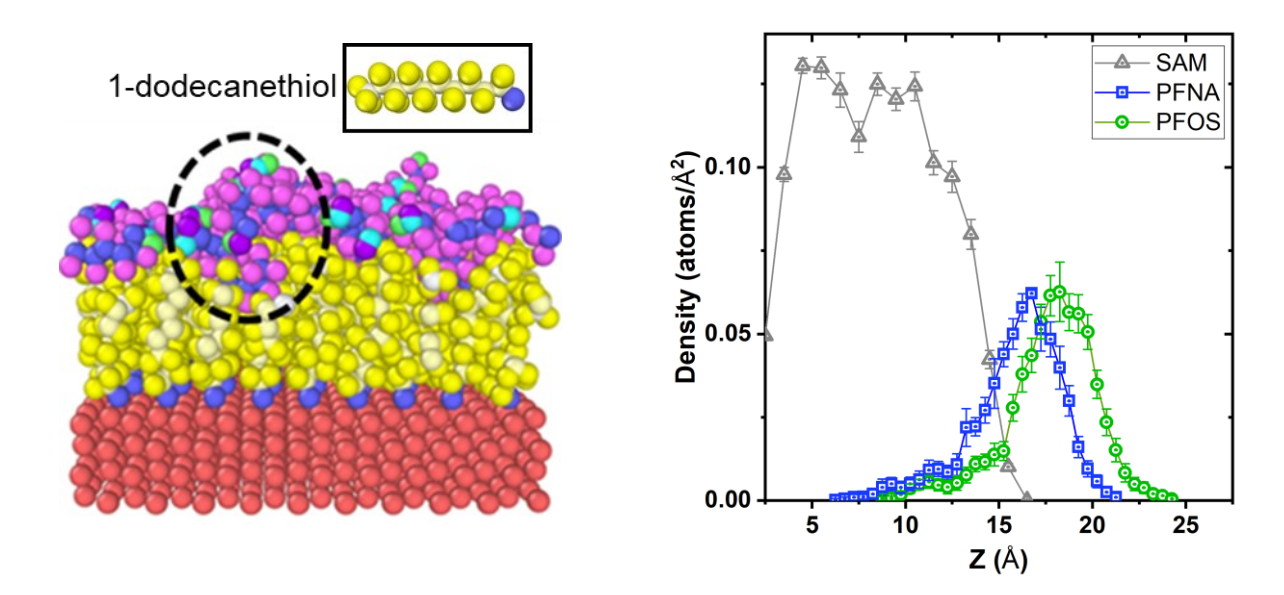


**Figure 7.** Molecular dynamics simulation of PFNA/PFOS interactions with CH<sub>3</sub>-terminated SAM. Top-view snapshots for **(a)** PFNA and **(b)** PFOS and the corresponding 2D density plots for **(c)** PFNA and **(d)** PFOS. Side-view snapshot for **(e)** PFNA molecules at the SAM interface showing the insertion of the fluorocarbon tail into the SAM. **(f)** Z-direction density profiles of atoms of SAM and adsorbed PFNA/PFOS molecules at the end of the simulation (additional profiles shown in SI 11). All images are obtained after equilibrating the system when approached with initial tail-down PFNA/PFOS orientation. Additional videos on the adsorption process of PFNA/PFOS molecules are presented in the SI 12.

510

		Eqn. (2)		Eqn. (3)				Eqn. (4)		
	$m_C = \frac{m_{\text{max,L}} * K_L * C}{1 + K_L * C}$			$m_{C} = \frac{m_{\text{max,G}} * K_{G}C^{n_{g}}}{1 + K_{G}C^{n_{g}}}$				$m_{C} = K_{F} * C^{\frac{1}{n_{f}}}$		
	$m_{max, L}$	$K_L$	$\chi^2$	<b>m</b> <sub>max, G</sub>	$K_G$	$n_g$	$\chi^2$	$K_F$	$n_f$	$\chi^2$
	$(ng cm^{-2})$	$(L\ mg^{-1})$		(ng cm <sup>-2</sup> )	$(Lmg^{-1})^{n_g} \\$			$(\operatorname{ng} \operatorname{cm}^{-2} \operatorname{L}^{\frac{1}{\operatorname{n_f}}} \operatorname{mg}^{-\frac{1}{\operatorname{n_f}}})$	)	
PFNA	428 ± 48	$(5.8 \pm 1.7) \times 10^{-3}$	1244	$362 \pm 68$	$(2.0 \pm 3.8) \times 10^{-3}$	1.30 ± 0.5	1305	$17.5 \pm 7.0$	2.1 ± 0.3	1547
PFOS	$244 \pm 38$	$(5.2 \pm 2.0)$ × $10^{-3}$	642	191 ± 36	$(0.78 \pm 2.0) \times 10^{-3}$	1.5 ± 0.6	654	$8.3 \pm 4.4$	2.0 ± 0.4	772

**Table 2.** Kinetic model fitting parameters for PFNA or PFOS adsorption on CH<sub>3</sub>-terminated SAM using the linearized Avrami model.

	Concentration	$n_{av_1}$	$k_{av_1}$	$R^2$	$n_{av_2}$	$k_{av_2}$	$R^2$
	$(mg L^{-1})$		$(min^{-n_{av}}) \\$			$\left(min^{-n_{av}}\right)$	
PFNA	50	1.64	0.034	0.94	0.67	0.31	0.87
	500	2	0.025	0.99	0.86	0.29	0.98
PFOS	50	1.62	0.044	0.99	0.30	1.13	0.63
	500	1.97	0.024	0.99	0.67	0.49	0.82

- Askeland, M., Clarke, B.O., Cheema, S.A., Mendez, A., Gasco, G. and Paz-Ferreiro, J. 2020. Biochar sorption of PFOS, PFOA, PFHxS and PFHxA in two soils with contrasting texture. Chemosphere 249, 126072.
- Avrami, M. 1939. Kinetics of phase change. I General theory. The Journal of Chemical Physics 7(12), 1103-1112.
- Avrami, M. 1940. Kinetics of phase change. II Transformation time relations for random distribution of nuclei. The Journal of Chemical Physics 8(2), 212-224.
- Avrami, M. 1941. Granulation, phase change, and microstructure kinetics of phase change. III. The Journal of Chemical Physics 9(2), 177-184.
  - Barzen-Hanson, K.A., Davis, S.E., Kleber, M. and Field, J.A. 2017. Sorption of fluorotelomer sulfonates, fluorotelomer sulfonamido betaines, and a fluorotelomer sulfonamido amine in national foam aqueous film-forming foam to soil. Environmental Science & Technology 51(21), 12394-12404.
  - Beltran-Heredia, J. and Sanchez-Martin, J. 2009. Removal of sodium lauryl sulphate by coagulation/flocculation with Moringa oleifera seed extract. J. Hazard. Mater. 164(2-3), 713-719.
  - Boyer, T.H., Fang, Y.D., Ellis, A., Dietz, R., Choi, Y.J., Schaefer, C.E., Higgins, C.P. and Strathmann, T.J. 2021. Anion exchange resin removal of per- and polyfluoroalkyl substances (PFAS) from impacted water: A critical review. Water Research 200.
  - Brusseau, M.L., Anderson, R.H. and Guo, B. 2020. PFAS concentrations in soils: Background levels versus contaminated sites. Sci. Total Environ. 740.
  - Buck, R.C., Franklin, J., Berger, U., Conder, J.M., Cousins, I.T., De Voogt, P., Jensen, A.A., Kannan, K., Mabury, S.A. and van Leeuwen, S.P. 2011. Perfluoroalkyl and polyfluoroalkyl substances in the environment: terminology, classification, and origins. Integrated Environmental Assessment and Management 7(4), 513-541.
  - Butt, H.J. and Jaschke, M. 1995. Calculation of thermal noise in Atomic Force Microscopy. Nanotechnology 6(1), 1-7.
  - Cai, W.W., Navarro, D.A., Du, J., Ying, G.G., Yang, B., McLaughlin, M.J. and Kookana, R.S. 2022. Increasing ionic strength and valency of cations enhance sorption through hydrophobic interactions of PFAS with soil surfaces. Sci. Total Environ. 817.
  - CDC 2019 US Department of Health and Human Services Centers for Disease Control and Prevention: Fourth National Report on Human Exposure to Environmental Chemicals.
  - Cestari, A.R., Vieira, E.F.S., Lopes, E.C.N. and da Silva, R.G. 2004. Kinetics and equilibrium parameters of Hg(II) adsorption on silica-dithizone. Journal of Colloid and Interface Science 272(2), 271-276.
  - Cestari, A.R., Vieira, E.F.S., Pinto, A.A. and Lopes, E.C.N. 2005. Multistep adsorption of anionic dyes on silica/chitosan hybrid 1. Comparative kinetic data from liquid- and solid-phase models. Journal of Colloid and Interface Science 292(2), 363-372.
  - Choudhary, A., Dong, D.P., Tsianou, M., Alexandridis, P. and Bedrov, D. 2022. Adsorption Mechanism of Perfluorooctanoate on Cyclodextrin-Based Polymers: Probing the Synergy of Electrostatic and Hydrophobic Interactions with Molecular Dynamics Simulations. ACS Materials Letters 4(5), 853-859.
  - Conder, J.M., Hoke, R.A., De Wolf, W., Russell, M.H. and Buck, R.C. 2008. Are PFCAs bioaccumulative? A critical review and comparison with regulatory lipophilic compounds. Environmental Science & Technology 42(4), 995-1003.
- Deng, S.B., Nie, Y., Du, Z.W., Huang, Q., Meng, P.P., Wang, B., Huang, J. and Yu, G. 2015. Enhanced adsorption of perfluorooctane sulfonate and perfluorooctanoate by bamboo-derived granular activated carbon. J. Hazard. Mater. 282, 150-157.
- Deng, S.B., Zhang, Q.Y., Nie, Y., Wei, H.R., Wang, B., Huang, J., Yu, G. and Xing, B.S. 2012. Sorption mechanisms of perfluorinated compounds on carbon nanotubes. Environ. Pollut. 168, 138-144.

- Djilani, C., Zaghdoudi, R., Modarressi, A., Rogalski, M., Djazi, F. and Lallam, A. 2012. Elimination of
   organic micropollutants by adsorption on activated carbon prepared from agricultural waste.
   Chemical Engineering Journal 189, 203-212.
- Du, Z.W., Deng, S.B., Bei, Y., Huang, Q., Wang, B., Huang, J. and Yu, G. 2014. Adsorption behavior and
   mechanism of perfluorinated compounds on various adsorbents-A review. J. Hazard. Mater. 274,
   443-454.
- Ebrahimi, F., Lewis, A.J., Sales, C.M., Suri, R. and McKenzie, E.R. 2021. Linking PFAS partitioning behavior in sewage solids to the solid characteristics, solution chemistry, and treatment processes. Chemosphere 271.

- Evich, M.G., Davis, M.J.B., McCord, J.P., Acrey, B., Awkerman, J.A., Knappe, D.R.U., Lindstrom, A.B., Speth, T.F., Tebes-Stevens, C., Strynar, M.J., Wang, Z.Y., Weber, E.J., Henderson, W.M. and Washington, J.W. 2022. Per- and polyfluoroalkyl substances in the environment. Science 375(6580), 512-+.
  - Fitzgerald, N.J.M., Wargenau, A., Sorenson, C., Pedersen, J., Tufenkj, N., Novak, P.J. and Simcik, M.F. 2018. Partitioning and Accumulation of Perfluoroalkyl Substances in Model Lipid Bilayers and Bacteria. Environmental Science & Technology 52(18), 10433-10440.
  - Freundlich, H. 1907. Über die adsorption in lösungen. Zeitschrift für physikalische Chemie 57(1), 385-470.
- Gagliano, E., Sgroi, M., Falciglia, P.P., Vagliasindi, F.G.A. and Roccaro, P. 2020. Removal of poly- and perfluoroalkyl substances (PFAS) from water by adsorption: Role of PFAS chain length, effect of organic matter and challenges in adsorbent regeneration. Water Research 171, 115381.
- Gao, X. and Chorover, J. 2012. Adsorption of perfluorooctanoic acid and perfluorooctanesulfonic acid to iron oxide surfaces as studied by flow-through ATR-FTIR spectroscopy. Journal of Environemntal Chemistry 9(2), 148-157.
- Guelfo, J.L. and Higgins, C.P. 2013. Subsurface Transport Potential of Perfluoroalkyl Acids at Aqueous Film-Forming Foam (AFFF)-Impacted Sites. Environmental Science & Technology 47(9), 4164-4171.
- Higgins, C.P. and Luthy, R.G. 2006. Sorption of perfluorinated surfactants on sediments. Environmental Science & Technology 40(23), 7251-7256.
- Huang, X.C., Li, C., Zuo, K.C. and Li, Q.L. 2020. Predominant Effect of Material Surface Hydrophobicity on Gypsum Scale Formation. Environmental Science & Technology 54(23), 15395-15404.
- Jeon, J., Kannan, K., Lim, B.J., An, K.G. and Kim, S.D. 2011. Effects of salinity and organic matter on the partitioning of perfluoroalkyl acid (PFAs) to clay particles. Journal of Environmental Monitoring 13(6), 1803-1810.
- Jiang, X.Z., Wang, W., Yu, G. and Deng, S.B. 2021. Contribution of Nanobubbles for PFAS Adsorption on Graphene and OH- and NH2-Functionalized Graphene: Comparing Simulations with Experimental Results. Environmental Science & Technology 55(19), 13254-13263.
- Johnson, R.L., Anschutz, A.J., Smolen, J.M., Simcik, M.F. and Penn, R.L. 2007. The adsorption of perfluorooctane sulfonate onto sand, clay, and iron oxide surfaces. Journal of Chemical and Engineering Data 52(4), 1165-1170.
- Jorgensen, W.L., Maxwell, D.S. and Tirado-Rives, J. 1996. Development and testing of the OPLS allatom force field on conformational energetics and properties of organic liquids. Journal of the American Chemical Society 118(45), 11225-11236.
- Jorgensen, W.L. and Tirado-Rives, J. 1988. The OPLS [optimized potentials for liquid simulations] potential functions for proteins, energy minimizations for crystals of cyclic peptides and crambin. Journal of the American Chemical Society 110(6), 1657-1666.
- Kancharla, S., Dong, D.P., Bedrov, D., Alexandridis, P. and Tsianou, M. 2022. Binding of Perfluorooctanoate to Poly(ethylene oxide). Macromolecules 55(11), 4624-4636.
- Kou, J. and Xu, S.H. 2016. In situ kinetics and conformation studies of dodecylamine adsorption onto zinc sulfide using a quartz crystal microbalance with dissipation (QCM-D). Colloids and Surfaces a-Physicochemical and Engineering Aspects 490, 110-120.

- Kunieda, H. and Shinoda, K. 1976. Krafft points, critical micelle concentrations, surface tension, and solubilizing power of aqueous solutions of fluorinated surfactants. The Journal of Physical Chemistry 80(22), 2468-2470.
- Langmuir, I. 1918. The adsorption of gases on plane surfaces of glass, mica and platinum. Journal of the American Chemical Society 40(9), 1361-1403.
- Lee, H. and Mabury, S.A. 2017. Sorption of perfluoroalkyl phosphonates and perfluoroalkyl phosphinates in soils. Environmental Science & Technology 51(6), 3197-3205.
- Li, D., Londhe, K., Chi, K., Lee, C.S., Venkatesan, A.K. and Hsiao, B.S. 2021. Functionalized bioadsorbents for removal of perfluoroalkyl substances: A perspective. AWWA Water Science 3(6), e1258.
- Li, F., Fang, X.L., Zhou, Z.M., Liao, X.B., Zou, J., Yuan, B.L. and Sun, W.J. 2019. Adsorption of perfluorinated acids onto soils: Kinetics, isotherms, and influences of soil properties. Sci. Total Environ. 649, 504-514.
- Li, Y.S., Oliver, D.P. and Kookana, R.S. 2018. A critical analysis of published data to discern the role of soil and sediment properties in determining sorption of per and polyfluoroalkyl substances (PFASs). Sci. Total Environ. 628-629, 110-120.
- Liu, W., Lin, T., Zhang, X., Jiang, F.C., Yan, X.S. and Chen, H. 2022. Adsorption of perfluoroalkyl acids on granular activated carbon supported chitosan: Role of nanobubbles. Chemosphere 309.
- Loganathan, N. and Wilson, A.K. 2022. Adsorption, Structure, and Dynamics of Short- and Long-Chain PFAS Molecules in Kaolinite: Molecular-Level Insights. Environmental Science & Technology 56(12), 8043-8052.

636 637

638 639

640

641

642

643 644

645

646 647

648

649 650

- Lopes, E.C.N., dos Anjos, F.S.C., Vieira, E.F.S. and Cestari, A.R. 2003. An alternative Avrami equation to evaluate kinetic parameters of the interaction of Hg(11) with thin chitosan membranes. Journal of Colloid and Interface Science 263(2), 542-547.
- Lyu, X.Y., Xiao, F., Shen, C.Y., Chen, J.J., Park, C.M., Sun, Y.Y., Flury, M. and Wang, D.J. 2022. Perand Polyfluoroalkyl Substances (PFAS) in Subsurface Environments: Occurrence, Fate, Transport, and Research Prospect. Reviews of Geophysics 60(3).
- Lyu, Y., Brusseau, M.L., Chen, W., Yan, N., Fu, X.R. and Lin, X.Y. 2018. Adsorption of PFOA at the Air-Water Interface during Transport in Unsaturated Porous Media. Environmental Science & Technology 52(14), 7745-7753.
- Mahinroosta, R. and Senevirathna, L. 2020. A review of the emerging treatment technologies for PFAS contaminated soils. Journal of Environmental Management 255.
- McCleaf, P., Englund, S., Ostlund, A., Lindegren, K., Wiberg, K. and Ahrens, L. 2017. Removal efficiency of multiple poly- and perfluoroalkyl substances (PFASs) in drinking water using granular activated carbon (GAC) and anion exchange (AE) column tests. Water Research 120, 77-87.
- Meng, P.P., Deng, S.B., Lu, X.Y., Du, Z.W., Wang, B., Huang, J., Wang, Y.J., Yu, G. and Xing, B.S. 2014. Role of Air Bubbles Overlooked in the Adsorption of Perfluorooctanesulfonate on Hydrophobic Carbonaceous Adsorbents. Environmental Science & Technology 48(23), 13785-13792.
- Milinovic, J., Lacorte, S., Vidal, M. and Rigol, A. 2015. Sorption behaviour of perfluoroalkyl substances in soils. Sci. Total Environ. 511, 63-71.
- Moody, C.A. and Field, J.A. 2000. Perfluorinated surfactants and the environmental implications of their use in fire-fighting foams. Environmental Science & Technology 34(18), 3864-3870.
- Nagasawa, D., Azuma, T., Noguchi, H., Uosaki, K. and Takai, M. 2015. Role of Interfacial Water in Protein Adsorption onto Polymer Brushes as Studied by SFG Spectroscopy and QCM. Journal of Physical Chemistry C 119(30), 17193-17201.
- Nalam, P.C., Pham, A., Castillo, R.V. and Espinosa-Marzal, R.M. 2019. Adsorption Behavior and Nanotribology of Amine-Based Friction Modifiers on Steel Surfaces. Journal of Physical Chemistry C 123(22), 13672-13680.
- Nguyen, L.A.T., Schwarze, M. and Schomacker, R. 2015. Adsorption of non-ionic surfactant from aqueous solution onto various ultrafiltration membranes. Journal of Membrane Science 493, 120-133.

- Nguyen, T.M.H., Braunig, J., Thompson, K., Thompson, J., Kabiri, S., Navarro, D.A., Kookana, R.S., Grimison, C., Barnes, C.M., Higgins, C.P., McLaughlin, M.J. and Mueller, J.F. 2020. Influences of Chemical Properties, Soil Properties, and Solution pH on Soil-Water Partitioning Coefficients of Per- and Polyfluoroalkyl Substances (PFASs). Environmental Science & Technology 54(24), 15883-15892.
- 670 O'Hagan, D. 2008. Understanding organofluorine chemistry. An introduction to the C-F bond. Chemical Society Reviews 37(2), 308-319.
- Pan, G. and You, C. 2010. Sediment-water distribution of perfluorooctane sulfonate (PFOS) in Yangtze River Estuary. Environ. Pollut. 158(5), 1363-1367.

- Pereira, H.C., Ullberg, M., Kleja, D.B., Gustafsson, J.P. and Ahrens, L. 2018. Sorption of perfluoroalkyl substances (PFASs) to an organic soil horizon Effect of cation composition and pH. Chemosphere 207, 183-191.
- Plimpton, S. 1995. Fast Parallel Algorithms for Short-Range Molecular Dynamics. Journal of Computational Physics 117(1), 1-19.
- Qian, J., Shen, M., Wang, P., Wang, C., Hou, J., Ao, Y., Liu, J. and Li, K. 2017. Adsorption of perfluorooctane sulfonate on soils: Effects of soil characteristics and phosphate competition. Chemosphere 168, 1383-1388.
- Reth, M., Berger, U., Broman, D., Cousins, I.T., Nilsson, E.D. and McLachlan, M.S. 2011. Water-to-air transfer of perfluorinated carboxylates and sulfonates in a sea spray simulator. Environmental Chemistry 8(4), 381-388.
- Royer, B., Cardoso, N.F., Lima, E.C., Vaghetti, J.C.P., Simon, N.M., Calvete, T. and Veses, R.C. 2009. Applications of Brazilian pine-fruit shell in natural and carbonized forms as adsorbents to removal of methylene blue from aqueous solutions-Kinetic and equilibrium study. J. Hazard. Mater. 164(2-3), 1213-1222.
- Siow, K.S., Britcher, L., Kumar, S. and Griesser, H.J. 2019. QCM-D and XPS study of protein adsorption on plasma polymers with sulfonate and phosphonate surface groups. Colloids and Surfaces B-Biointerfaces 173, 447-453.
- Sunderland, E.M., Hu, X.D.C., Dassuncao, C., Tokranov, A.K., Wagner, C.C. and Allen, J.G. 2019. A review of the pathways of human exposure to poly- and perfluoroalkyl substances (PFASs) and present understanding of health effects. Journal of Exposure Science and Environmental Epidemiology 29(2), 131-147.
- Thibaut, A., Misselyn-Bauduin, A.M., Grandjean, J., Broze, G. and Jerome, R. 2000. Adsorption of an aqueous mixture of surfactants on silica. Langmuir 16(24), 9192-9198.
- Thompson, A.P., Aktulga, H.M., Berger, R., Bolintineanu, D.S., Brown, W.M., Crozier, P.S., in 't Veld, P.J., Kohlmeyer, A., Moore, S.G., Nguyen, T.D., Shan, R., Stevens, M.J., Tranchida, J., Trott, C. and Plimpton, S.J. 2022. LAMMPS a flexible simulation tool for particle-based materials modeling at the atomic, meso, and continuum scales. Computer Physics Communications 271, 108171.
- Torres, F.J., Ochoa-Herrera, V., Blowers, P. and Sierra-Alvarez, R. 2009. Ab initio study of the structural, electronic, and thermodynamic properties of linear perfluorooctane sulfonate (PFOS) and its branched isomers. Chemosphere 76(8), 1143-1149.
- Vargas, A.M.M., Cazetta, A.L., Kunita, M.H., Silva, T.L. and Almeida, V.C. 2011. Adsorption of methylene blue on activated carbon produced from flamboyant pods (Delonix regia): Study of adsorption isotherms and kinetic models. Chemical Engineering Journal 168(2), 722-730.
- Vericat, C., Vela, M.E. and Salvarezza, R.C. 2005. Self-assembled monolayers of alkanethiols on Au(111):
   surface structures, defects and dynamics. Physical Chemistry Chemical Physics 7(18), 3258-3268.
- Vieira, E.F.S., Cestari, A.R., Lopes, E.C.N., Barreto, L.S., Lazaro, G.S. and Almeida, L.E. 2007.

  Determination of kinetic parameters from isothermal calorimetry for interaction processes of pyrimethamine with chitosan derivatives. Reactive & Functional Polymers 67(9), 820-827.

- 714 Vu, C.T. and Wu, T.T. 2022. Recent progress in adsorptive removal of per- and poly-fluoroalkyl substances (PFAS) from water/wastewater. Critical Reviews in Environmental Science and Technology 52(1), 90-129.
- Walczyk, W. and Schonherr, H. 2014. Characterization of the interaction between AFM tips and surface nanobubbles. Langmuir 30(24), 7112-7126.
- Wang, F., Shih, K.M. and Leckie, J.O. 2015. Effect of humic acid on the sorption of perfluorooctane sulfonate (PFOS) and perfluorobutane sulfonate (PFBS) on boehmite. Chemosphere 118, 213-218.
- Wang, M.C., Orr, A.A., Jakubowski, J.M., Bird, K.E., Casey, C.M., Hearon, S.E., Tamamis, P. and Phillips,
   T.D. 2021. Enhanced adsorption of per- and polyfluoroalkyl substances (PFAS) by edible,
   nutrient-amended montmorillonite clays. Water Research 188.

728 729

730

731

732

733

734

735

736

737

738

739

740

744

745

746

747

- Wang, X.Y., Zhao, B.Y., Hu, J., Wang, S., Tai, R.Z., Gao, X.Y. and Zhang, L.J. 2017. Interfacial gas nanobubbles or oil nanodroplets? Physical Chemistry Chemical Physics 19(2), 1108-1114.
- Wei, C.L., Song, X., Wang, Q. and Hu, Z.H. 2017. Sorption kinetics, isotherms and mechanisms of PFOS
   on soils with different physicochemical properties. Ecotox. Environ. Safe. 142, 40-50.
  - Willemsen, J.A.R. and Bourg, I.C. 2021. Molecular dynamics simulation of the adsorption of per- and polyfluoroalkyl substances (PFASs) on smectite clay. Journal of Colloid and Interface Science 585, 337-346.
  - Wu, J.J., Contreras, A.E. and Li, Q.L. 2014. Studying the impact of RO membrane surface functional groups on alginate fouling in seawater desalination. Journal of Membrane Science 458, 120-127.
  - Yan, B., Munoz, G., Sauve, S. and Liu, J.X. 2020. Molecular mechanisms of per- and polyfluoroalkyl substances on a modified clay: a combined experimental and molecular simulation study. Water Research 184.
  - Yan, B., Wang, J. and Liu, J.X. 2021. STXM-XANES and computational investigations of adsorption of per- and polyfluoroalkyl substances on modified clay. Water Research 201.
  - You, C., Jia, C.X. and Pan, G. 2010. Effect of salinity and sediment characteristics on the sorption and desorption of perfluorooctane sulfonate at sediment-water interface. Environ. Pollut. 158(5), 1343-1347.
- Yu, Q., Zhang, R.Q., Deng, S.B., Huang, J. and Yu, G. 2009. Sorption of perfluorooctane sulfonate and perfluorooctanoate on activated carbons and resin: Kinetic and isotherm study. Water Research 43(4), 1150-1158.
  - Zeng, T.Z., Kim, K.T., Werth, C.J., Katz, L.E. and Mohanty, K.K. 2020. Surfactant Adsorption on Shale Samples: Experiments and an Additive Model. Energy & Fuels 34(5), 5436-5443.
    - Zhang, C., Yan, H., Li, F., Hu, X. and Zhou, Q. 2013. Sorption of short- and long-chain perfluoroalkyl surfactants on sewage sludges. J. Hazard. Mater. 260, 689-699.
    - Zhang, D.Q., Zhang, W.L. and Liang, Y.N. 2019. Adsorption of perfluoroalkyl and polyfluoroalkyl substances (PFASs) from aqueous solution A review. Sci. Total Environ. 694, 133606.
- Zhang, Q., Deng, S., Yu, G. and Huang, J. 2011. Removal of perfluorooctane sulfonate from aqueous
   solution by crosslinked chitosan beads: Sorption kinetics and uptake mechanism. Bioresource
   Technology 102(3), 2265-2271.
- Zhang, R.M., Yan, W. and Jing, C.Y. 2014. Mechanistic study of PFOS adsorption on kaolinite and montmorillonite. Colloids and Surfaces A-Physicochemical and Engineering Aspects 462, 252-258.
- Zhang, W., Yang, H., Liu, F.H., Chen, T., Hu, G.X., Guo, D.H., Hou, Q.F., Wu, X., Su, Y. and Wang, J.B.
   Molecular interactions between DOPA and surfaces with different functional groups: a chemical force microscopy study. Rsc Advances 7(52), 32518-32527.
- Zhao, L.X., Bian, J.N., Zhang, Y.H., Zhu, L.Y. and Liu, Z.T. 2014. Comparison of the sorption behaviors
   and mechanisms of perfluorosulfonates and, perfluorocarboxylic acids on three kinds of clay
   minerals. Chemosphere 114, 51-58.
- Zheng, L.W., Gao, Y.C., Du, J.H., Zhang, W., Huang, Y.J., Zhao, Q.Q., Duan, L.C., Liu, Y.J., Naidu, R.
   and Pan, X.L. 2021. Single and Binary Adsorption Behaviour and Mechanisms of Cd2+, Cu2+
   and Ni2+ onto Modified Biochar in Aqueous Solutions. Processes 9(10).

Zhou, Q., Deng, S.B., Yu, Q., Zhang, Q.Y., Yu, G., Huang, J. and He, H.P. 2010. Sorption of perfluorooctane sulfonate on organo-montmorillonites. Chemosphere 78(6), 688-694.
Zhu, B.Y. and Gu, T.R. 1991. Surfactant Adsorption at Solid Liquid Interfaces. Advances in Colloid and Interface Science 37(1-2), 1-32.